







First Detection of Interaction between a Magnetic Disk Wind and an Episodic Jet in a Protostellar System

Chin-Fei Lee^{1,2} , Benoit Tabone^{3,4}, Sylvie Cabrit⁴ , Claudio Codella^{5,6} , Linda Podio⁵, Jonathan Ferreira⁶ , and Jonatan Jacquemin-Ide⁶

¹ Academia Sinica Institute of Astronomy and Astrophysics, No. 1, Sec. 4, Roosevelt Road, Taipei 10617, Taiwan

² Graduate Institute of Astronomy and Astrophysics, National Taiwan University, No. 1, Sec. 4, Roosevelt Road, Taipei 10617, Taiwan

³ Leiden Observatory, Leiden University, PO Box 9513, 2300 RA Leiden, The Netherlands

⁴ Observatoire de Paris, PSL University, Sorbonne Université, CNRS, LERMA, 61 Av. de l'Observatoire, F-75014 Paris, France

⁵ INAF, Osservatorio Astrofisico di Arcetri, Largo E. Fermi 5, I-50125 Firenze, Italy

⁶ Univ. Grenoble Alpes, CNRS, Institut de Planétologie et d'Astrophysique de Grenoble (IPAG), F-38000 Grenoble, France

Received 2020 December 13; revised 2020 December 29; accepted 2021 January 8; published 2021 February 2

Abstract

Rotating outflows from protostellar disks might trace extended magnetohydrodynamic (MHD) disk winds (DWs), providing a solution to the angular momentum problem in disk accretion for star formation. In the jet system HH 212, a rotating outflow was detected in SO around an episodic jet detected in SiO. Here we spatially resolve this SO outflow into three components: a collimated jet aligned with the SiO jet, the wide-angle disk outflow, and an evacuated cavity in between created by a large jet-driven bow shock. Although it was theoretically predicted, this is the first time that such a jet–DW interaction has been directly observed and resolved, and it is crucial for the proper interpretation and modeling of non-resolved DW candidates. The resolved kinematics and brightness distribution both support the wide-angle outflow to be an extended MHD DW dominating the local angular momentum extraction out to 40 au, but with an inner launching radius truncated to $\gtrsim 4$ au. Inside 4 au, where the DW may not exist, the magnetorotational instability might be transporting angular momentum outward. The jet–DW interaction in HH 212, potentially present in other similar systems, opens an entirely new avenue to probe the large-scale magnetic field in protostellar disks.

Unified Astronomy Thesaurus concepts: [Accretion \(14\)](#); [Star formation \(1569\)](#); [Jets \(870\)](#); [Herbig-Haro objects \(722\)](#); [Young stellar objects \(1834\)](#); [Stellar jets \(1607\)](#)

1. Introduction

Rotating outflows from protostellar disks are a newly discovered component in star formation (Launhardt et al. 2009; Greenhill et al. 2013; Zapata et al. 2015; Bjerkeli et al. 2016; Hirota et al. 2017; Tabone et al. 2017; Lee et al. 2018b, 2018c; Louvet et al. 2018; Zhang et al. 2018; de Valon et al. 2020). They might trace extended magnetohydrodynamic (MHD) disk winds (DWs), providing a solution to the angular momentum problem in disk accretion. The HH 212 protostellar system (Zinnecker et al. 1992) is a young system located in Orion at ~ 400 pc, harboring a nearly edge-on rotating disk optimal for detecting such an extended DW. The central protostar has a mass of $0.25 \pm 0.05 M_{\odot}$, deeply embedded in an infalling-rotating envelope (Lee et al. 2017c). Previous Atacama Large Millimeter/submillimeter Array (ALMA) observations have spatially resolved the disk (Lee et al. 2017b), which is rotating within a centrifugal barrier at ~ 44 au (Lee et al. 2017c). A spinning jet was also detected in SiO carrying angular momentum away from the innermost disk at a radius of ~ 0.05 – 0.20 au (Lee et al. 2017a; Tabone et al. 2017), allowing disk material to fall onto the protostar. Dust polarization was also detected toward the disk, suggesting a presence of a poloidal magnetic field that could launch a DW around the jet (Lee et al. 2018a).

A slow wide-angle outflow was indeed detected in SO and SO₂ at 60 au resolution, rotating in the same sense as the disk, and consistent with an extended MHD DW launched from ~ 0.1 to 40 au that extracts enough angular momentum to drive disk accretion (Tabone et al. 2017). Later observations at ~ 4 times higher resolution resolved SO emission into a collimated

jet and a wide-angle rotating shell (Lee et al. 2018b). Now with new ALMA observations about two times deeper and a spatial resolution of ~ 13 au ($0''.033$), we retrieve additional SO emission structures reconciling the above seemingly contradictory results, providing a confirmation for an extended DW as well as the first evidence of jet–DW interaction first predicted by Tabone et al. (2018). This interaction provides unique first clues to the unknown magnetic field strength and distribution in young protostellar disks. The current central bottleneck in our understanding of planet formation is the underlying structure of protoplanetary disks, and in particular the role of MHD DWs in mass and angular momentum removal (see Raymond & Morbidelli 2020 for a recent review).

2. Observations

HH 212 was observed with ALMA in Band 7 centered at a frequency of ~ 341.5 GHz on 2017 November 27 in Cycle 5 (Project ID: 2017.1.00044.S). As the observations and calibrations have been reported in Lee et al. (2019), here we only report important information related to the SO line at 346.528481 GHz and the SiO line at 347.330631 GHz. Three scheduling blocks were executed with an on-source time of 98 minutes. The projected baselines were ~ 60 – 8500 m. We set up the correlator to have three continuum windows and one spectral window. The SiO and SO lines were both included in the spectral window, which has a velocity resolution of ~ 1.69 km s^{−1} per channel.

The *uv* data was calibrated manually by the ALMA QA2 team using the Common Astronomy Software Applications (CASA) package version 5.1.1. No self-calibration was

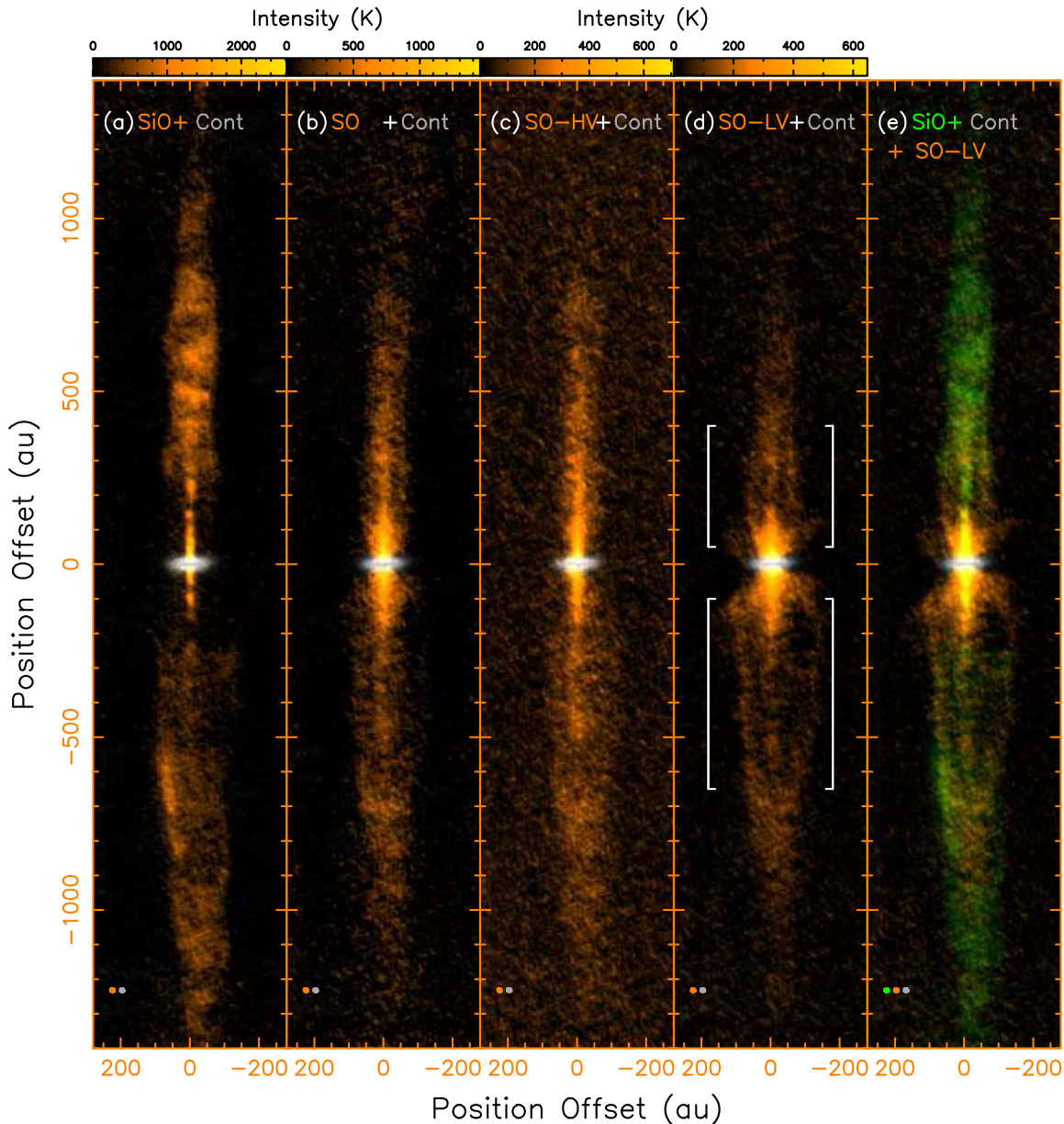


Figure 1. SiO and SO intensity maps toward the HH 212 system within 1400 au of the protostar, together with the 350 GHz continuum map of the disk (gray image adopted from Lee et al. 2019). The maps are all rotated by 22.5° clockwise to align the jet axis in the north–south direction. SO-HV indicates the SO map at high velocity more than $\pm 3 \text{ km s}^{-1}$ away from the systemic velocity. SO-LV indicates the SO map at low velocity within $\pm 3 \text{ km s}^{-1}$ of the systemic velocity. Color codes are the same as the labels. White brackets mark the shells.

performed due to insufficient signal-to-noise ratio of the continuum data in the long baselines. A robust factor of 0.5 was used for the visibility weighting to generate SO and SiO channel maps with a synthesized beam of $0''.036 \times 0''.030$ at a position angle of $\sim -78^\circ$ and a noise level of $\sim 0.75 \text{ mJy beam}^{-1}$ (7.0 K). We also included the SO visibility data obtained in Cycle 3 (Lee et al. 2018b) and reduced the noise level slightly down to $0.67 \text{ mJy beam}^{-1}$ (6.2 K) in the SO channel maps. The velocities in the channel maps are local standard of rest (LSR) velocities.

3. Results

Figure 1 shows the SO map in comparison to the SiO map of the jet and the continuum map of the dusty disk (adopted from Lee et al. 2019) within 1400 au of the central protostar at 13 au

resolution. SiO shows an episodic jet launched from the innermost disk, appearing first as a highly collimated chain of knots in inner 200 au and then a chain of broader bow shocks downstream at larger distances. SO also shows a jet aligned with the SiO jet.

We can unveil the wide-angle outflow by separating the SO emission into two velocity components. At high velocity (more than $\pm 3 \text{ km s}^{-1}$ away from the systemic velocity of $\sim 1.7 \text{ km s}^{-1}$, Figure 1(c)), SO traces a collimated jet aligned with the SiO jet, but wider possibly because the SO line has a lower critical density than SiO and thus can trace less dense material. The critical densities (in H_2) are $7.2 \times 10^6 \text{ cm}^{-3}$ for SO and $1.2 \times 10^7 \text{ cm}^{-3}$ for SiO (Schöier et al. 2005). At low velocity (within $\pm 3 \text{ km s}^{-1}$ of the systemic velocity, Figure 1(d)), thin outflow shells (marked with white brackets) are detected in SO surrounding the jet. Only their bases were detected before (Lee

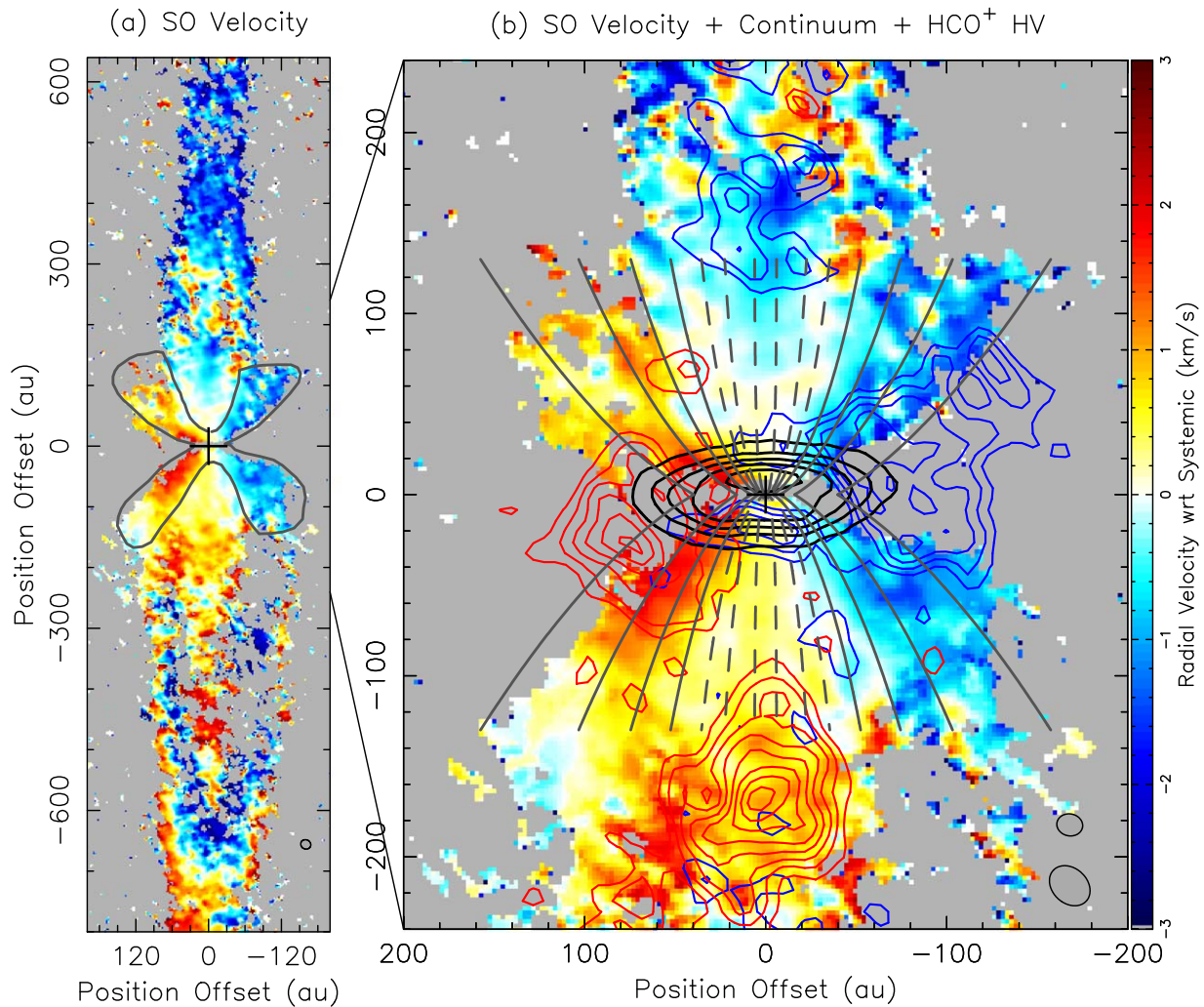


Figure 2. Intensity-weighted velocity maps of SO in the inner region at low velocity. The gray X-shaped curve in (a) outlines the wide-angle rotating outflow detected in SO. Panel (b) zooms into the central region. Black contours show the same disk map as in Figure 1. Red and blue contours show the high-velocity (HV) HCO⁺ emission adopted from Lee et al. (2017c), outlining the boundary of the innermost envelope. Gray curves plot the streamlines of the disk wind in Model L5W30, with footpoints at $r_0 = 4, 8, 16,$ and 40 au. Dashed curves show the streamlines with footpoints at $r_0 = 0.2, 1, 2$ au.

et al. 2018b). They are now detected further away and seen to smoothly connect to the SiO/SO bow shocks downstream at larger distances (~ 600 au; Figure 1(e)). Faint extended SO emission is also detected surrounding the base of the shells, within $z \lesssim 150$ au from the disk. This emission shows up better in an intensity-weighted velocity map (Figure 2), forming a wide-angle rotating outflow together with the base of the shells, appearing as a thick X-shape fanning out from the disk, rotating around the jet. Away from the base, the shells are mainly blueshifted in the north and redshifted in the south, similar to the velocity sense of the bow shocks at larger distance and thus driven by them. The inner part of the wide-angle outflow coincides with the base of the shells and is thus perturbed by the bow shocks. The wide-angle outflow has an outer boundary outlined by the inner infalling-rotating envelope traced by the high-velocity emission of HCO⁺ (Figure 2(b)), confirming that it originates from the disk. Its outer part is unperturbed by the bow shocks, providing the best opportunity to check the previously proposed MHD DW interpretation (Tabone et al. 2017, 2020).

4. MHD DW Model

Various MHD models are being developed to launch DWs and carry away part or all of the angular momentum from accretion disks (Turner et al. 2014; Bai 2017; Zhu & Stone 2018; Riols et al. 2020). The first and most simple 2D version of these models is a steady-state, axisymmetric, self-similar wind launched from a geometrically thin Keplerian disk (Blandford & Payne 1982; Ferreira 1997). These models are well suited for comparison with observations because they allow for parameter studies. As discussed in Tabone et al. (2020), the observable structure and kinematics of the wind in these models are mainly determined by three parameters: (1) protostellar mass M_* defining the Keplerian rotation $v_{k,0} = \sqrt{GM_*/r_0}$ at a radius r_0 in the disk; (2) magnetic level arm parameter $\lambda \simeq (r_A/r_0)^2$, where r_A is the Alfvén radius along the streamline launched from a footpoint at r_0 , determining the poloidal acceleration and the extracted specific angular momentum (in particular, the terminal wind velocity and the final specific angular momentum achieved along each streamline are $v_w \sim v_{k,0}\sqrt{2\lambda-3}$ and $l \sim \lambda l_0$, respectively, where $l_0 = r_0 v_{k,0}$ is the value at the footpoint at r_0); and (3) widening factor $W \equiv r_{\max}/r_0$, where r_{\max} is the maximum

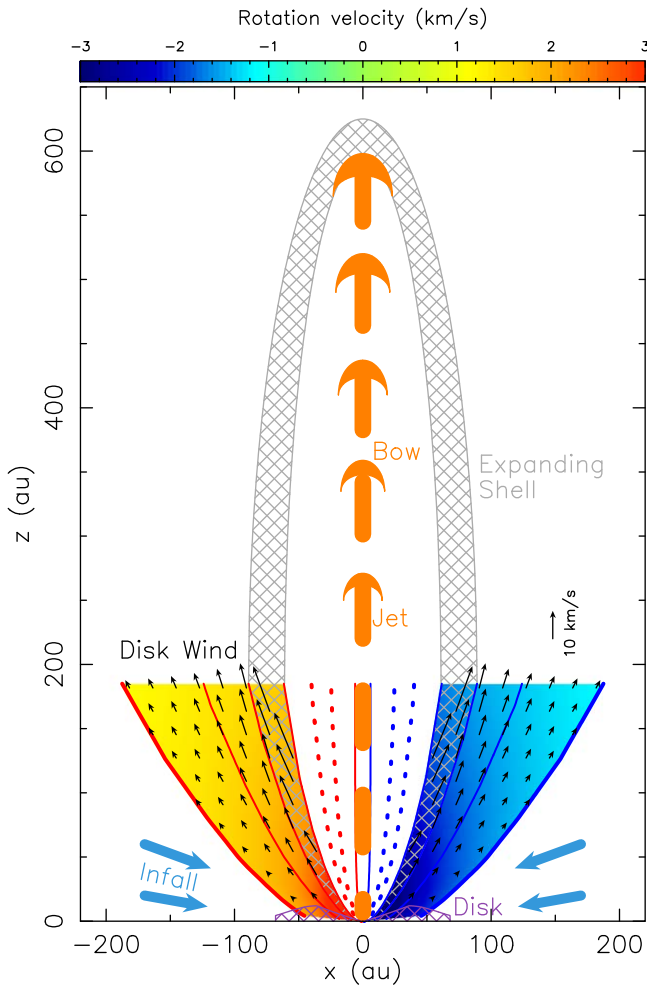


Figure 3. Schematic diagram showing the extended disk wind and jet in our model, and the interaction between them. The wind has a launching radius of 4 to 40 au, while the jet has a launching radius of 0.05–0.20 au. The shell (gray cross-hatched region) extends from the inner part of the wind to the jet-driven bow shock. The rotation velocity (color image) and outflow velocity (vectors) in the wind are derived from Model L5W30, with the outflow velocity in the inner part replaced with a radially expanding velocity.

radius reached by the streamline at large distance, controlling the flow transverse size.

Assuming $M_* \sim 0.2M_\odot$, Tabone et al. (2017, 2020) found their DW Model L5W30 (with $\lambda \sim 5.5$ and $W \sim 30$) to broadly reproduce the transverse spatio-kinematic structure of the SO rotating outflow, with $r_0 = 0.1\text{--}40$ au. The same model is thus adopted here to compare with the SO wide-angle outflow resolved at higher resolution and sensitivity. As shown in Figure 2(b), the wide-angle outflow shows an opening structure in good agreement with the predicted model streamlines but with a launching radius truncated to $\gtrsim 4$ au. We thus assume an extended DW with a launching radius of $r_0 \sim 4\text{--}40$ au for the wide-angle outflow, as shown in Figure 3. The wind is assumed to be symmetric with respect to the disk midplane and extend out to 185 au to the north and south. The inner part of the wind bounded by the model streamlines launched from 4 to 8 au roughly coincides with the base of the shells (Figure 2(b)) and is thus assumed to become the shell perturbed by the bow shocks, with its outflow velocity replaced by a radially expanding velocity $v_r = r/t_s$, where t_s is the dynamical age of the shell (Lee et al. 2018b). We assume a temperature of 100 K

in the outer unperturbed part and 200 K in the inner perturbed part (shell), based on the temperatures derived before for the disk atmosphere and the shells (Lee et al. 2018b). The SO jet is assumed to have a launching radius of 0.10–0.20 au in the dust-free zone (Tabone et al. 2020). It has a temperature of 300 K, which is a mean value adopted before to derive the SO abundance (Podio et al. 2015). As the observed jet is unresolved, this jet component is only for illustrative purposes.

In this self-similar model, the disk has an accretion rate varying with radius as

$$\dot{M}_{\text{acc}}(r_0) = \dot{M}_{\text{in}} \left(\frac{r_0}{r_{\text{in}}} \right)^\xi \quad (1)$$

with \dot{M}_{in} being the accretion rate at the inner radius r_{in} and ξ being the ejection efficiency (Ferreira & Pelletier 1995). Thus, the mass-loss rate in the wind between the inner radius r_{in} and outer radius r_{out} will be

$$\dot{M}_{\text{DW}} = \dot{M}_{\text{out}} - \dot{M}_{\text{in}} = \dot{M}_{\text{in}} \left[\left(\frac{r_{\text{out}}}{r_{\text{in}}} \right)^\xi - 1 \right] \quad (2)$$

where \dot{M}_{out} is the accretion rates at r_{out} . For the disk wind to remove all of the accretion angular momentum, we have (Tabone et al. 2020)

$$\xi \sim \frac{1}{2(\lambda - 1)}. \quad (3)$$

With $\lambda \sim 5.5$, $r_{\text{out}} \sim 40$ au, $r_{\text{in}} \sim 4$ au, and $\dot{M}_{\text{in}} \sim 3 \times 10^{-6} M_\odot \text{ yr}^{-1}$ (Lee 2020), we have $\dot{M}_{\text{DW}} \sim 0.9 \times 10^{-6} M_\odot \text{ yr}^{-1}$. Along each streamline, the corresponding wind density has been given in Tabone et al. (2020).

This model can be compared quantitatively to the observed wide-angle outflow in terms of kinematics. A radiative transfer code (Lee et al. 2014) adding the SO line is used to generate the position–velocity (PV) diagrams of the SO emission from the model, assuming local thermodynamic equilibrium (LTE). The SO abundance (wrt molecular hydrogen) x_{SO} is a free parameter to be derived by matching the observed intensity. Within 100 au of the protostar, because the jet has a proper motion of $\sim 64 \text{ km s}^{-1}$ (Claussen et al. 1998) and a mean radial velocity of $\sim -3.7 \text{ km s}^{-1}$ in the northern component and $\sim 2.5 \text{ km s}^{-1}$ in the southern component (Lee et al. 2017a), the inclination angles of the wide-angle outflow and jet are assumed to be $\sim -3^\circ$ in the northern component and $\sim 2^\circ$ in the southern component.

Figure 4 shows the resulting model PV diagrams on the observed ones cut across the jet axis centered at increasing distance from the protostar to near the end of the wide-angle outflow, with $x_{\text{SO}} \sim 4.5 \times 10^{-7}$ in the extended DW and $x_{\text{SO}} \sim 6.2 \times 10^{-5}$ in the jet. As can be seen, with the outer unperturbed part of the wind, this model roughly reproduces the PV structures of the faint unperturbed wide-angle outflow (marked with blue brackets), even though it predicts a rotation velocity slightly larger than observed. Note that the wide-angle outflow in the north is only detected within ~ 130 au of the protostar (see also Figure 2). Moreover, with the inner part of the wind being radially expanding, the model produces tilted elliptical PV structures for the shell and can roughly match the observations with the dynamical age $t_s \sim 37$ yr, similar to that found in Lee et al. (2018b). The resulting outflow velocity is drawn in Figure 3. This age roughly agrees with the axial

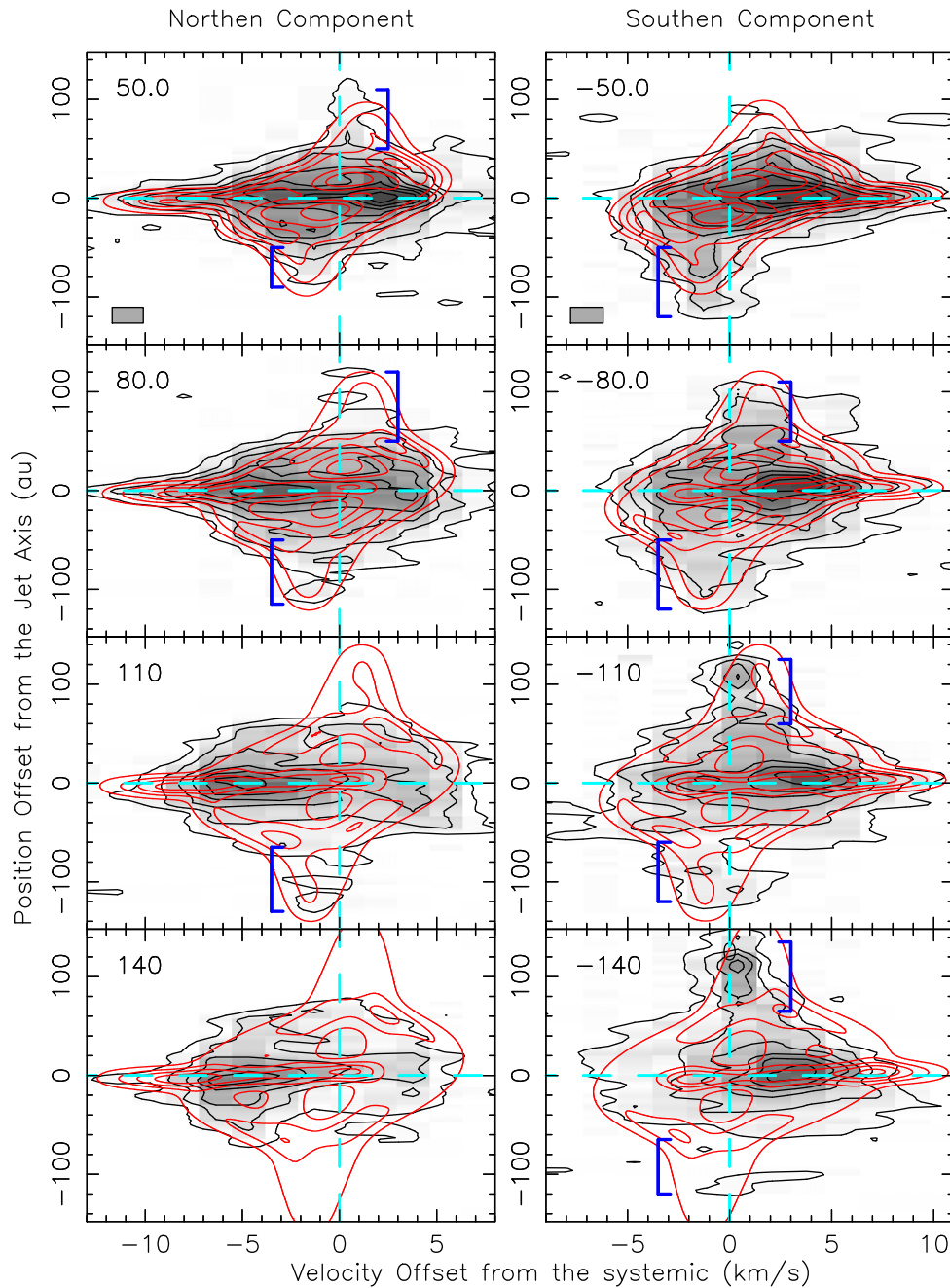


Figure 4. Comparison of model PV diagrams (red contours) to the observed PV diagrams (black contours) of SO emission cut across the jet axis centered at increasing distances (as indicated in the upper-left corners in au) from the protostar along the jet axis. Contours start at 2σ with a step of 3σ , where $\sigma \sim 4.5$ K. Blue brackets mark the regions where the unperturbed wide-angle outflow is detected. The bright emission near the jet axis is from the jet. The emission in between the jet and the unperturbed wide-angle outflow is from the shells.

distance (~ 600 au) traveled by the cavity apex for a jet speed ~ 64 km s $^{-1}$, supporting that the shell at the base is created by the same large jet bow shock seen downstream. However, as the model PV structures of the shell are tilted more than observed, the rotation velocity in the shell is also over-predicted. Note that the density in the shell is ~ 4 times that in the unperturbed disk-wind model in order to match the observed SO intensity there. The model can produce linear PV structures for the jet with a broad range of velocities near the jet axis, also roughly consistent with the observations.

In order to obtain a better match to the observed rotation in the wide-angle outflow, we reduce the rotation velocity and

poloidal velocity in the model by lowering the λ value, keeping the same for the other parameters. At the same time, we decrease the inner launch radius of the SO jet to 0.05 au to maintain the same maximum jet velocity. As shown in Figure 5, this very simple “modified” model with $\lambda \sim 3.5$ provides a better match to the observations. Such a low λ value is favored by recent MHD simulations including stellar irradiation (Wang et al. 2019). Moreover, with this smaller λ , the wind density will be a factor of ~ 3 higher and thus the required SO abundance will become $\simeq 10^{-7}$, close to that in the HH 212 disk (Podio et al. 2015). This result is in excellent agreement with thermo-chemical modeling of dense Class 0

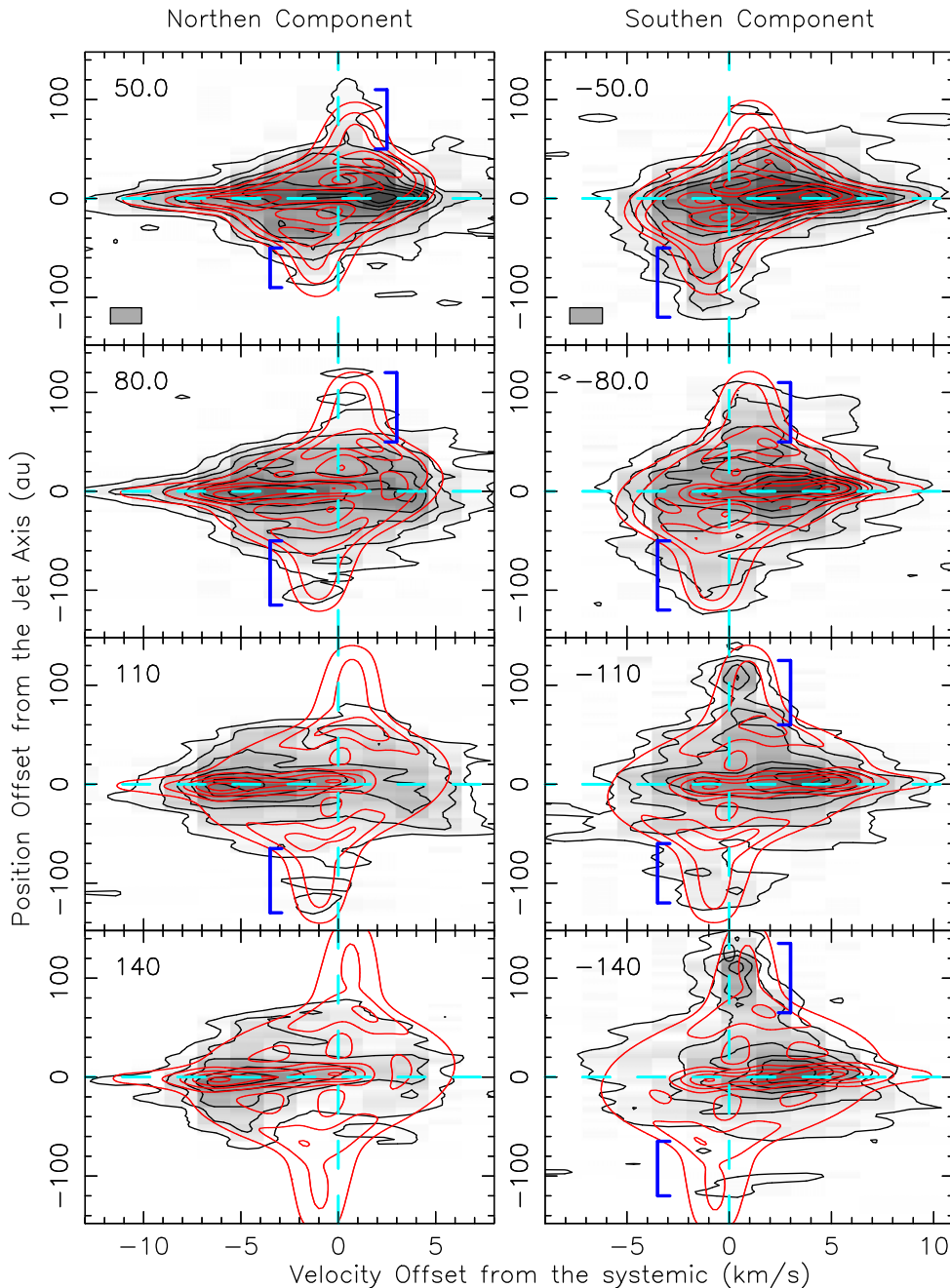


Figure 5. Same as Figure 4 but with a smaller $\lambda \sim 3.5$ in order to better reproduce the rotation velocity of the wide-angle outflow including the shells.

MHD DWs (Panoglou et al. 2012), which predicts that the SO wind abundance should remain “frozen” near the disk value up to $z \simeq 100$ au. The sudden drop of the wind SO brightness observed above $z \sim 150$ au (Figures 1 and 2) is also predicted by this model, as the wind becomes transparent to photo-dissociating far-ultraviolet photons from the accretion shock (Panoglou et al. 2012). The DW is thus dense enough to remove the disk angular momentum, if its SO abundance is close to that in the disk.

5. Conclusions

Our new observations have reconciled previous studies of SO rotating outflow in HH 212, supporting the presence of an extended MHD DW out to the disk outer edge at 40 au,

removing most of the angular momentum flux required for accretion (Tabone et al. 2017, 2020), but with a smaller magnetic level arm and an inner launching radius truncated to $\gtrsim 4$ au. This extended wind is likely a steady wind continuously ejected from the disk. However, the SO and SiO jet is resolved as a chain of knots, most likely caused by time variations in the jet ejection velocity (Eisloffel & Mundt 1992). In particular, three different periods of ejections have been estimated for the knots and bow shocks (Lee 2020). This, in turn, could be due to episodic accretion near the innermost disk, triggered by gravitational instability (Vorobyov et al. 2018), a binary companion, and/or a star–disk interaction. The jet from the innermost disk ($r_0 \sim 0.05\text{--}0.20$ au) drives large bow shocks interacting with the extended DW and producing a cavity, with the thin SO shell forming its boundary. These data are thus

providing the first unambiguous evidence for the theoretically predicted interaction between a time-variable jet and an outer DW (Tabone et al. 2018). Resolving such an interaction is crucial for the proper interpretation and modeling of less well-resolved DW candidates.

Furthermore, the width of the cavity provides us with the first quantitative clues to the magnetic field strength in a DW. Indeed, the twisting of field lines at the base of MHD DWs creates a strong magnetic pressure that efficiently confines the sideways expansion of jets and jet bow shocks (Meliani et al. 2006; Matsakos et al. 2009). With a jet mass-flux $\sim 10^{-6} M_{\odot} \text{ yr}^{-1}$ ejected sideways at a speed $\sim 10 \text{ km s}^{-1}$ (Lee et al. 2015), and the magnetic field strength required in our wind model to drive accretion at $\dot{M}_{\text{in}} \sim 3 \times 10^{-6} M_{\odot} \text{ yr}^{-1}$, equilibrium at $z \sim 150 \text{ au}$ between the lateral ram pressure and magnetic pressure is reached on the streamline launched from 4 au, as observed. Hence, the cavity width appears consistent with the outer disk ($r_0 \geq 4 \text{ au}$) hosting a large-scale magnetic field sufficient to extract angular momentum at the observed rate. In addition, because magnetic pressure in self-similar MHD DWs increases inward faster ($\propto r_0^{-5/2}$) than the wind ram pressure (r^{-2}), the DW should be much weaker inside of $r_0 \sim 4 \text{ au}$, otherwise the bow shock could not have expanded that far. MHD numerical simulations of the jet/disk-wind interaction in HH 212 will be able to confirm and refine these results.

In the innermost disk with a radius of $\sim 0.2\text{--}4 \text{ au}$, another mechanism such as magnetorotational instability (MRI; Balbus & Hawley 2006) might thus be needed to transport disk angular momentum outward, allowing material to accrete to the innermost radius to the dust-free zone. Interestingly, 4 au is roughly of the same order as the predicted transition radius between the ionized inner disk (where MRI can grow) and the low-ionization external “non-ideal zone” (where the MRI is quenched by non-ideal MHD effects; Armitage 2011; Mori et al. 2019). Inside this radius, the disk surface temperature in HH 212 becomes $\gtrsim 1000 \text{ K}$ (Lee et al. 2017b) and thus MRI could turn on. A transition from an MHD disk-wind regime outside to an MRI-dominated regime inside is also predicted when disk magnetization decreases inward, due to, e.g., magnetic flux diffusion (Ferreira & Deguiran 2013). If confirmed, the transition suggested by our observations would then bring unique clues to ionization and field diffusion in young disks.

This paper makes use of the following ALMA data: ADS/JAO.ALMA#2017.1.00044.S. ALMA is a partnership of ESO (representing its member states), NSF (USA) and NINS (Japan), together with NRC (Canada), NSC and ASIAA (Taiwan), and KASI (Republic of Korea), in cooperation with the Republic of Chile. The Joint ALMA Observatory is operated by ESO, AUI/NRAO and NAOJ. C.-F.L. acknowledges grants from the Ministry of Science and Technology of Taiwan (MoST 107-2119-M-001-040-MY3) and the Academia Sinica (Investigator Award AS-IA-108-M01). B.T. acknowledges funding from the research program Dutch

Astrochemistry Network II with project number 614.001.751, which is financed by the Dutch Research Council (NWO). C.C. and L.P. acknowledge the project PRIN-INAF 2016 The Cradle of Life-GENESIS-SKA (General Conditions in Early Planetary Systems for the rise of life with SKA).

ORCID iDs

Chin-Fei Lee  <https://orcid.org/0000-0002-3024-5864>
 Sylvie Cabrit  <https://orcid.org/0000-0002-1593-3693>
 Claudio Codella  <https://orcid.org/0000-0003-1514-3074>
 Jonathan Ferreira  <https://orcid.org/0000-0002-7834-7341>

References

- Armitage, P. J. 2011, *ARA&A*, 49, 195
 Bai, X.-N. 2017, *ApJ*, 845, 75
 Balbus, S. A., & Hawley, J. F. 2006, *ApJ*, 652, 1020
 Bjerkeli, P., van der Wiel, M. H. D., Harsono, D., Ramsey, J. P., & Jørgensen, J. K. 2016, *Natur*, 540, 406
 Blandford, R. D., & Payne, D. G. 1982, *MNRAS*, 199, 883
 Claussen, M. J., Marvel, K. B., Wootten, A., & Wilking, B. A. 1998, *ApJL*, 507, L79
 de Valon, A., Dougados, C., Cabrit, S., et al. 2020, *A&A*, 634, L12
 Eisloeffel, J., & Mundt, R. 1992, *A&A*, 263, 292
 Ferreira, J., 1997, *A&A*, 319, 340
 Ferreira, J., & Deguiran, R. 2013, *HEDP*, 9, 67
 Ferreira, J., & Pelletier, G. 1995, *A&A*, 295, 807
 Greenhill, L. J., Goddi, C., Chandler, C. J., Matthews, L. D., & Humphreys, E. M. L. 2013, *ApJL*, 770, L32
 Hirota, T., Machida, M. N., Matsushita, Y., et al. 2017, *NatAs*, 1, 0146
 Launhardt, R., Pavlyuchenkov, Ya., Gueth, F., et al. 2009, *A&A*, 494, 147
 Lee, C.-F. 2020, *A&ARv*, 28, 1
 Lee, C.-F., Codella, C., Li, Z.-Y., et al. 2019, *ApJ*, 876, 63
 Lee, C.-F., Hirano, N., Zhang, Q., et al. 2014, *ApJ*, 786, 114
 Lee, C.-F., Hirano, N., Zhang, Q., et al. 2015, *ApJ*, 805, 186
 Lee, C.-F., Ho, P. T. P., Li, Z.-Y., et al. 2017a, *NatAs*, 1, 0152
 Lee, C.-F., Li, Z.-Y., Ching, T.-C., Lai, S.-P., & Yang, H. 2018a, *ApJ*, 854, 56
 Lee, C.-F., Li, Z.-Y., Codella, C., et al. 2018b, *ApJ*, 856, 14
 Lee, C.-F., Li, Z.-Y., Hirano, N., et al. 2018c, *ApJ*, 863, 94
 Lee, C.-F., Li, Z.-Y., Ho, P. T. P., et al. 2017b, *SciA*, 3, e1602935
 Lee, C.-F., Li, Z.-Y., Ho, P. T. P., et al. 2017c, *ApJ*, 843, 27
 Louvet, F., Dougados, C., Cabrit, S., et al. 2018, *A&A*, 618, A120
 Matsakos, T., Massaglia, S., Trussoni, E., et al. 2009, *A&A*, 502, 217
 Meliani, Z., Casse, F., & Sauty, C. 2006, *A&A*, 460, 1
 Mori, S., Bai, X.-N., & Okuzumi, S. 2019, *ApJ*, 872, 98
 Panoglou, D., Cabrit, S., Pineau des Forêts, G., et al. 2012, *A&A*, 538, A2
 Podio, L., Codella, C., Gueth, F., et al. 2015, *A&A*, 581, A85
 Raymond, S., & Morbidelli, A. 2020, arXiv:2002.05756
 Riols, A., Lesur, G., & Menard, F. 2020, *A&A*, 639, A95
 Schöier, F. L., van der Tak, F. F. S., van Dishoeck, E. F., et al. 2005, *A&A*, 432, 369
 Tabone, B., Cabrit, S., Bianchi, E., et al. 2017, *A&A*, 607, L6
 Tabone, B., Cabrit, S., Pineau des Forêts, G., et al. 2020, *A&A*, 640, A82
 Tabone, B., Raga, A., Cabrit, S., et al. 2018, *A&A*, 614, A119
 Turner, N. J., Fromang, S., Gammie, C., et al. 2014, in *Protostars and Planets VI*, ed. H. Beuther et al. (Tucson, AZ: Univ. Arizona Press), 411
 Vorobyov, E. I., Elbakyan, V. G., Plunkett, A. L., et al. 2018, *A&A*, 613, A18
 Wang, L., Bai, X.-N., & Goodman, J. 2019, *ApJ*, 874, 90
 Zapata, L. A., Lizano, S., Rodríguez, L. F., et al. 2015, *ApJ*, 798, 131
 Zhang, Y., Higuchi, A. E., Sakai, N., et al. 2018, *ApJ*, 864, 76
 Zhu, Z., & Stone, J. M. 2018, *ApJ*, 857, 34
 Zinnecker, H., Bastien, P., Arcoragi, J.-P., & Yorke, H. W. 1992, *A&A*, 265, 726